A regularized sparsity-promoting approach to eigenvalue decomposition polarization analysis in the time-frequency domain (RS-TFR)

Author One[a], Author Two[b], Author Three[a,b]

[a]*Department One, Address One, City One, 00000, State One, Country One*
[b]*Department Two, Address Two, City Two, 22222, State Two, Country Two*

Abstract

Polarization analysis is a signal processing tool for decomposing multi-component seismic signals to a set of rectilinearly or elliptically polarized elements. Theoretically, time-frequency (TF)-domain polarization methods are the most compatible tools for analyzing the intrinsically non-stationary seismic signals. The TF-domain polarization methods decompose the signal to a superposition of polarized elements with well-defined polarization properties, localized in the time and frequency domains. On the other hand, in practice, it suffers from a lack of resolution in the time and frequency, unable to discriminate between interfering seismic phases, and instability in the presence of noise, as they rely on a generally an underdetermined and low-resolution time-frequency representation (TFR) method.

Our contribution is threefold. Firstly, we rearrange the eigenvalue decomposition polarization analysis (EDPA) in the frequency domain, showing that the frequency-dependent polarization properties can be extracted from the Fourier coefficients by benefiting Fourier space orthogonality. Secondly, by extending from the frequency domain to the TF domain and combining with regularized sparsity-promoting time-frequency representation (RS-TFR), we alleviate the limited resolution in estimating the TF-domain polarization parameters. Thirdly and finally, by applying an adaptive regularized sparsity-promoting time-frequency filtering (RS-TFF), we extract and filter different phases of the seismic wave makes it possible to separate them. By applying the RS-TFF method on synthetic and real seismograms, we demonstrate the efficacy of the method in discriminating between the interfering seismic phases in time and frequency, including the body, Rayleigh, Love, and coda waves. The synthetic data corresponds to the source mechanism of $M_w = 6.7$ earthquake occurred at the Prince Edward Islands region, and the real dataset corresponds to the $M_w = 8.2$ earthquake occurred near the coast of Chiapas, Mexico.

Keywords: Eigenvalue decomposition, Polarization analysis and filtering, Sparsity-promoting inversion, Regularization, Reyleigh and Love waves, adaptive filtering, rectilinearity, directivity

1. Introduction

Seismic wavefield recorded as a seismogram is a superposition of overlapping direct, reflected, refracted, converted, and scattered body and surface waves, contaminated by various background sources and the signal generated noise [1, 20]. It is well known that surface and body waves can carry considerable information about the subsurface structure. Depending on the research scope, any of these seismic phases can be studied, while their detection and extraction based on their characteristics require advanced processing and analysis tools. In this way, multicomponent processing techniques have also been developed to analyze the nonlinear and time-varying processes behind the seismic sources and the propagating environment [Refer to [43] as a rigorous survey]. Among these techniques, polarization analysis and filtering methods have attracted significant attention.

Generally, the polarization analysis and filtering methods can be divided into three broad categories: time, frequency, and TF domain methods. As a pioneer, Flinn [12] introduced the eigenvalue decomposition polarization analysis in the time-domain. Likewise, Plešinger et al. [26] optimally extracted the polarization property by analyzing the signal in the Frenet Frame. By extending the method using Hilbert transform,

Vidale [42] introduced the analytic signal polarization technique. Although all these methods could extract the non-stationary signal properties by utilizing the time-windowing, they were not able to discriminate between overlapping events with different frequencies. Comparatively, studies were carried out on achieving polarization properties of the seismic time-series in the frequency domain. Primarily developed by [34], the direction of propagation of surface waves was obtained using the amplitude and phase information of different frequencies of seismic waves. Compatible to a pure state signal in the frequency domain, Samson and Olson [29] proposed a technique based on eigenvalue decomposition of the spectral matrix in different frequency bandwidths around a central frequency to provoke the polarization state of the signal. However, these techniques are incapable of the analysis of non-stationary signals in the time domain.

Due to the non-stationary nature of seismic signals with overlapping phases in time and frequency, pure time-domain or frequency-domain methods are often difficult to properly discriminate between the non-stationary seismic phases. To alleviate this, Jurkevics [17] proposed filtering the signals into a series of narrow frequency bands, applying short sliding time windows, and then estimating the polarization ellipse from the covariance matrix in each window at each band. Despite having a TF insight to polarization estimation, the resolution was still limited in the frequency domain due to the limited functionality of the bandpass filtering. Therefore, based on applying different TFR methods [3, 36, 40] and using various polarization estimation criteria, several TF-based polarization analysis methods were introduced for analyzing non-stationary seismic signals. These TF domain polarization estimation tools range from eigenvalue decomposition of covariance [18, 37] and complex trace analysis [42, 9, 31, 21, 33], to fitting the particle motion to a parametric polarization ellipse [24]. Despite attaining a TF domain estimations, these methods are not yet able to resolve closely-spaced overlapping seismic events in time and frequency.

Obtaining a high-resolution TFR have always been a challenge for the scientific community. To circumvent it, a variety of methods have been introduced, including synchrosqueezing transform (SST) [8], sparse transforms [7], RS-TFR [27, 14, 41], to name a few. Remarkably, by formulating the TFR as an inverse problem, and taking advantages of sparsity-promoting regularization as a promising tool to obtain a high-resolution solution, several methods have been developed to improve the resolution [27, 14, 41]. RS-TFR found many applications in seismology including the microseismic data denoising [41], attenuation estimates of propagating seismic waves [38], seismic ground roll attenuation [14].

On the other hand, polarization filtering techniques have also been developed to amplify or suppress different phases of seismic waves by using the analyzed polarization information. As pioneers, Flinn [12], Montalbetti and Kanasewich [23], Vidale [42] utilized time-domain rectilineary and directivity attributes to amplify body wave phases teleseismic data. Accordingly, Samson and Olson [29] applied these criteria to filter ultra low frequency magnetic field signal fluctuations in the frequency domain. Furthermore, Schimmel et al. [33] designed a TF domain filter based on the degree of polarization (DOP) extracted from the semi-major and semi-minor axis of the elliptical motion of the three component ambient noise data to filter the elliptical particle motion. Correspondingly, Pinnegar and Eaton [25], Pinnegar [24] utilized the semi-major, semi-minor, inclination, and azimuth parameters to discriminate between the circular and linear polarization to filer the Rayleigh waves. Although the filtering method was intuitive and innovative, he still faced challenges for filtering the linear phases as his method obtained a null value of azimuth and inclination parameters for linear particle motions.

This article begins with an in-detailed review of the formalism of the eigenvalue decomposition polarization analysis; we formulate the polarization properties by rearranging them as a function of frequency. On this basis, we obtain a high-resolution TF-based polarization properties by extending the formulation to the TF domain and using the RS-TFR. Furthermore, by extending the polarization filtering of Pinnegar [24] to incorporate TF information of directivity, rectilinearity, and amplitude obtained from the polarization analysis, we design a filter to accept or reject either the Linear and elliptical seismic phases. This paper is organized in the following manner. First, in section (2) we briefly review the theory behind the eigenvalue decomposition polarization analysis in the time, frequency, and TF domains. We show that the eigenvalue decomposition can be applied independently for every single frequency by taking advantage of the orthogonality of Fourier domain. This property can be extended to the TF domain, making it possible to obtain TF polarization parameters. Then, by reviewing the RS-TFR, we show that it gives a high-resolution TF map of the polarization parameters, making the eigenvalue decomposition stable in the presence of noise. Next,

2

in section ([3](#)) by conducting synthetic and real data examples, we show using a signal-adaptive polarization filtering algorithm based on the obtained TFR of polarization parameters, we can separate different phases of the seismic wave. Numerical experiments with synthetic and real earthquake data show that the RS-TFF approach when it combined with a properly defined polarization attributes is able to eliminate (or extract) different phases of seismic waves. Finally, in sections ([4](#)) and ([5](#)) we discuss the results and conclude the paper.

2. Theory

To keep this paper self-contained, we rearrange the formalism of the EDPA in the frequency and TF domain to be combined by RS-TFF. Furthermore, to have consistency with the numerical algorithms, we exclusively present a discrete version of the mathematical equations.

2.1. Polarization analysis using eigen-value decomposition

Suppose that

$$\boldsymbol{X} = [\boldsymbol{x}_1, \boldsymbol{x}_2, \boldsymbol{x}_3] \in \mathbb{R}^{L \times 3}, \tag{1}$$

is a seismic time-series recorded with three components aligned with the base vectors of a right-handed coordinate system $\{\boldsymbol{e}_E, \boldsymbol{e}_N, \boldsymbol{e}_Z\}$ (east-north-vertical), $\{\boldsymbol{e}_T, \boldsymbol{e}_R, \boldsymbol{e}_Z\}$ (transverse-radial-vertical), or $\{\boldsymbol{e}_L, \boldsymbol{e}_Q, \boldsymbol{e}_T\}$ (tangent-normal-binormal or Frenet wave). The latter coordinate systems are obtained from the ordinary east-north-vertical system by rotation [See [26] for more details]. Each component, $\boldsymbol{x}_i \in \mathbb{R}^{L \times 1}$ ($i = 1, 2, 3$), samples the wavefield arriving to the sensor along the time axis on $t_k = k\delta t$, with δt being sampling interval and $k = 0, 1, ..., 2n$ being the time index assuming an odd length $L = 2n + 1$ of seismogram.

Then, the polarization properties of $\boldsymbol{X}$ can be extracted by the eigenvalue decomposition of the covariance matrix

$$\boldsymbol{V} = \begin{bmatrix} V_{11} & V_{12} & V_{13} \\ V_{21} & V_{22} & V_{23} \\ V_{31} & V_{32} & V_{33} \end{bmatrix} \in \mathbb{R}^{3 \times 3} \tag{2}$$

[23, 12, 17, 16]. The elements of the symmetric and real-valued matrix $\boldsymbol{V}$ in Eq. ([2](#)) are auto- and cross-variances of the components of the time-series defined as

$$V_{ij} = \left[\frac{1}{2n+1} \sum_{l=0}^{2n} (x_i(l) - \mu_i)(x_j(l) - \mu_j) \right]. \tag{3}$$
$$i, j = 1, 2, 3$$

In Eq. ([3](#)), μ is the mean or expected value of components and is defined as

$$\mu_i = \Psi\{\boldsymbol{x}_i\} = \frac{1}{2n+1} \sum_{l=0}^{2n} x_i(l) \tag{4}$$

[23]. Assuming a weakly stationary condition for all the components of the time series, $\Psi\{\boldsymbol{x}_i\} \cong 0$, $i = 1, 2, 3$, Eq. ([3](#)) can be rewritten as

$$V_{ij} = \left[\frac{1}{2n+1} \sum_{l=0}^{2n} x_i(l) x_j(l) \right] = C_{ij}, \tag{5}$$

which simplifies the definition of elements in Eq. ([2](#)) to auto- and cross-correlations,

$$\boldsymbol{C} = \begin{bmatrix} C_{11} & C_{12} & C_{13} \\ C_{21} & C_{22} & C_{23} \\ C_{31} & C_{32} & C_{33} \end{bmatrix} \in \mathbb{R}^{3 \times 3}, \tag{6}$$

or equally,

$$C = \frac{\boldsymbol{X}^T\boldsymbol{X}}{N}, \tag{7}$$

where $(.)^T$ in Eq. (7) denotes the transposition operator. The weakly stationary assumption in Eq. (5) is satisfied by applying DC removal or detrending.

The quadratic matrix of correlation coefficient, $\boldsymbol{C}$, fits the particle motion elipsoid in a least-squares sense; the parameters of this elipsoid are obtained by solving the system of equations

$$(\mathbf{C} - \lambda_i\mathbf{I})\mathbf{u} = 0. \tag{8}$$

Geometrically, solutions to Eq. (8) give directions that the linear transformation $\boldsymbol{C}$ merely elongates or shrinks (the eigenvectors, ($\boldsymbol{u}_1$, $\boldsymbol{u}_2$, $\boldsymbol{u}_3$), and the amount that they elongate/shrink (eigenvalues, (λ_1, λ_2, λ_3), and the eigenvectors direct the base vectors of the polarization motion ellipsoid. The eigenvalues are sorted such that $\lambda_j \geq \lambda_k$ for $j < k$.

2.1.1. Eigenvalue decomposition in the frequency domain

The first implementations of the eigenvalue decomposition on frequency domain were proposed by [28, 29]; the spectral matrix corresponds to a perturbation around the central frequency $[\omega - \delta\omega, \omega + \delta\omega]$ was decomposed using eigenvalue decomposition to provoke the polarization states of the signal. This decomposition scheme is more compatible with natural signals, which are rarely composed of single-frequency polarized elements. However, by decomposing to a strictly polarized single frequency state, one can benefit from the orthogonality of the Fourier transform to extract frequency-dependent polarization properties. Here, we review and simplify the process.

The discrete Fourier domain counterpart of Eq. (1), $\boldsymbol{X}^f = \boldsymbol{\mathcal{FT}}\{[\boldsymbol{x}_1, \boldsymbol{x}_2, \boldsymbol{x}_3]\} = [\boldsymbol{f}_1, \boldsymbol{f}_2, \boldsymbol{f}_3] \in \mathbb{R}^{L\times 3}$, is obtained by modulating $\boldsymbol{x}_i$, $i = 1, 2, 3$, with pure sinusoids having discrete frequencies as follows

$$f_i(l) = \frac{1}{2n+1}\sum_{k=0}^{2n}x_i(k)exp(\frac{-2\pi \jmath kl}{2n+1}), \ i = 1, 2, 3. \tag{9}$$

Here, $l = -n, ..., n$, is the frequency index giving frequency content of the signal on discrete frequencies $\omega_l = \frac{l}{(2n+1)\delta t}$, and $\jmath$ is the imaginary symbol. The original signal is reconstructed by applying the inverse Fourier transform, $\boldsymbol{X} = \boldsymbol{\mathcal{IFT}}\{[\boldsymbol{f}_1, \boldsymbol{f}_2, \boldsymbol{f}_3]\}$,

$$x_i(k) = \sum_{l=0}^{2n}f_i(l)exp(\frac{2\pi \jmath kl}{2n+1}), \ i = 1, 2, 3. \tag{10}$$

The frequency-domain counterpart of Eq. (5) is defined as

$$C_{ij} = ZL\{\boldsymbol{\mathcal{IFT}}\{\langle\boldsymbol{f}_i, \boldsymbol{f}_j^*\rangle\}\}, \tag{11}$$

in which, $(.)^*$, and $\langle.,.\rangle$ are complex conjugate operator, and inner product, respectively, and $ZL\{.\}$ is a function that picks the zero-lag element. By taking advantage of the orthogonality property of the Fourier domain, Eq. (11) can be written as

$$C_{ij} = \sum_{l=0}^{n}C_{ij}(l) = \sum_{l=0}^{n}ZL\{\boldsymbol{\mathcal{IFT}}\{\langle\hat{\boldsymbol{f}}_i^l, \hat{\boldsymbol{f}}_j^{l*}\rangle\}\}, \tag{12}$$

with

$$\hat{f}_k^l(j) = \begin{cases} f_k(j) & j = l \\ 0 & j \neq l \end{cases} \tag{13}$$

4

Hence, the auto- and cross-correlation terms for every single frequency can be decomposed via Eq. (13). Instead of applying operation in Eq. (13) to obtain $C_{ij}(l)$, it is attainable from the inner product terms $\boldsymbol{g}_{ij} = \langle \boldsymbol{f}_i, \boldsymbol{f}_j^* \rangle$. Then,

$$C_{ij}(l) = \begin{cases} g_{ij}(-l) + g_{ij}(l) & l \neq 0 \\ g_{ij}(l) & l = 0 \end{cases}, \; l = 0, 1, ..., n \tag{14}$$

gives the frequency-dependent auto- and cross-correlation elements. Solving system of equations (8) for the frequency-dependent elements $C_{ij}(l)$,

$$(\mathbf{C}(l) - \lambda_i(l)\mathbf{I})\mathbf{u}(l) = 0, \tag{15}$$

gives the eigenvectors, $(\boldsymbol{u}_1(l), \boldsymbol{u}_2(l) \; \boldsymbol{u}_3(l))$ and eigenvalues, $(\lambda_1(l), \lambda_2(l), \lambda_3(l))$, as a function of frequency.

2.1.2. Eigenvalue decomposition in the time-frequency domain

The process described in section (2.1.1) effectively decomposes stationary signals into it's frequency-dependent polarization components (eigenvectors and eigenvalues). Having to deal with seismic data's nonstationary nature, the same definition is extended to give polarization components that depend on time and frequency by substituting a TFR in place of the ordinary Fourier transform. Accordingly, many researchers devoted to finding efficient time-frequency analysis methods, and many powerful methods have been developed in the past several decades, including the wavelet transform [22], the Wigner-Ville distribution [11], short time fourier transform (STFT) [3], Stockwell transform (ST) [36], etc. As an instance, the STFT representation of the $\boldsymbol{x}_i$ in Eq. (1) is obtained by

$$TF_{STFT}(k,l) = \sum_{\hat{k}=0}^{2n} x(\hat{k}) e^{-\pi(\hat{k}-k)^2/\sigma^2} exp(\frac{-2\pi j \hat{k} l}{2n+1}),$$
$$l = -n, ..., -1, 0, 1, ..., 2n, \; k = 0, 1, ..., 2n \tag{16}$$

with $e^{-\pi(\hat{k}-k)^2/\sigma^2}$ being a Gaussian window with standard deviation σ centered around k index. The definition in Eq. (16) can be extended to the ST [36] by applying a time–frequency spectral localization uding a window function scalable with frequency as

$$TF_{ST}(k,l) = \sum_{\hat{k}=0}^{2n} x(\hat{k}) |l| e^{-\pi l^2 (\hat{k}-k)^2} exp(\frac{-2\pi j \hat{k} l}{2n+1}), \tag{17}$$

with k and l are defined the same as Eq. (16).

Correspondingly, Wavelet transform (WT) methods gives time-scale representation (TSR) of the signal, and can be convertable to the TFR [35]. By obtaining TF of the 3-components of the signal, the TF-domain Auto- and cross-correlation terms is obatained as

$$C_{ij}(k,l) = \begin{cases} g_{ij}(k,-l) + g_{ij}(k,l) & l \neq 0 \\ g_{ij}(k,l) & l = 0 \end{cases} \tag{18}$$

for time and frequency indexes , $k = 0, 1, ..., 2n + 1, \; l = 0, 1, ..., n$. Consequently, the TF-dependent eigenvectors, $(\boldsymbol{u}_1(k,l), \boldsymbol{u}_2(k,l) \; \boldsymbol{u}_3(k,l))$ and eigenvalues, $(\lambda_1(k,l), \lambda_2(k,l), \lambda_3(k,l))$, is obtained by solving

$$(\mathbf{C}(k,l) - \lambda_i(k,l)\mathbf{I})\mathbf{u}(k,l) = 0, \tag{19}$$

giving a TF map of polarization state of signal. This decomposition process is similar to the method introduced by Pinnegar [24]. However, as we will discuss in the following sections, it can be used to filter the linearly polarized seismic phases, which is not achieved with the Pinnegar [24] method.

5

2.2. Regularized sparsity-promoting TF decomposition

The system of equations for STFT and ST a linear system. By rearrangement of eqs. 16 and 17, the $\boldsymbol{x}$ in Eq. (1) is decomposed to the TF coefficients as a system of equations

$$\boldsymbol{x} = \boldsymbol{G}I, \qquad \boldsymbol{G} \in \mathbb{R}^{L \times L^2}, \qquad I \in \mathbb{R}^{L^2 \times 1} \qquad (20)$$

where I is a vectorized rearrangement of TF array in eqs. 16 and 17, or WT coefficients [See [41, 14] for more details about the structure of the forward operator $\boldsymbol{G}$]. Infinite number of solutions fits Eq. (20) due to an under-determined nature of the systems. Obviously, the maximum likelihood solution to Eq. (20)

$$\boldsymbol{I}_{LS} = \arg \min_{\boldsymbol{I}} \left\{ \frac{1}{2} ||\boldsymbol{G}I - \boldsymbol{x}||_2^2 \right\}, \qquad (21)$$

may not be a good estimation of the original model because it is very sensitive to data errors, due to the underdetermined nature of the $\boldsymbol{G}$ operator. Instead, to obtain a statble while desired solution, some form of a priori information about the original model is added to Eq. (21). Restoration processes in this way are studied under the name of regularization techniques [39]. A sparsity-promoting regularization enables selecting an $\boldsymbol{I}$ model with a minimum number of non-zero coefficient by solving a constrained optimization problem

$$\boldsymbol{I}_R = \arg \min_{\boldsymbol{I}} \left\{ \frac{1}{2} ||\boldsymbol{G}I - \boldsymbol{x}||_2^2 \ \ s.t. \ \ ||\boldsymbol{I}||^1 < \epsilon \right\}, \qquad (22)$$

where $||\boldsymbol{I}||^1 = \sum_i |I(i)|$ is the ℓ_1 norm of a vector $\boldsymbol{x}$ and ϵ is a user-specified bound for the error in the data [41, 14]. The parameter ϵ controls the sparsity of the $\boldsymbol{I}$ coefficients. As $\epsilon \to 0$, the solution of Eq. (22) converges to the sparsest solution. On the other hands, as $\epsilon \to \inf$, the solution of Eq. (22) converges to the solution of 21. By this strategy and by choosing a proper ϵ, one can control the resolution of estimating the $\boldsymbol{I}$ coefficient. It provides the possibility to attain a high-resolution TFR of the signal being able to discriminate between closely spaced events in time and frequency, while fitting reconstructing the data in the sense of Eq. (20). The problem 22, can be written in an unconstrained form as

$$\boldsymbol{I}_R = \arg \min_{\boldsymbol{I}} \left\{ \frac{1}{2} ||\boldsymbol{G}I - \boldsymbol{x}||_2^2 + \lambda ||\boldsymbol{I}||^1 \right\}, \qquad (23)$$

by suitably defining a lagrangian muliplier λ according to the Karush–Kuhn–Tucker (KKT) condition [19].

The constrained optimization problem 22 or it's unconstrained equivalent 23 can be solved by a variety of methods. One practical way to solve 23 is the method [15]. The iteratively reweighted least squares (IRLS) algorithm solves a sequence of weighted least-squares problems whose solution converges to the solution of the original problem. Another efficient algorithm to solve 22 based on the split Bregman method was introduced by [14] in which Bregman iterative regularization solves a sequence of convex problems which converges to the solution of the original problem. In like manner, a fast and efficient algorithm was introduced by [41] to solve 23 based on fast iterative soft thresholding algorithm (FISTA) [4] which does not need matrix inversion and is very fast for high-dimensional problems.

The obtained RS-TFR through eqs. 22 or 23 is utilized to design an adaptive filtering for extract (or filtering) different phases of seismic waves. In the next section, we briefly review the adaptive filtering approach in the TF domain.

2.3. Adaptive filtering in the TF domain

Adaptive filtering has already been applied by [23], [42], and [17] in the time domain. Schimmel et al. [33] took benefit of the planarity attribute to filter the Rayleigh waves from the ambient noise data in the TF domain. In a very intuitive scheme, Pinnegar [24] utilized the combination of Inclination, azimuth, and rectilinearity attributes in the TF domain to filter the Reyleigh waves.

However, his method was not able to analyze the pure linear polarization as in introduced polarization analysis method the inclination was undefined for linear motions [See section 3 for more details]. Here, we develop an algorithm by extending the rectilinearity and directivity attributes introduced by [17] and [23] from time to the TF plane; then, by using a similar scheme introduced by [24] we combine the attributes to construct the adaptive rejection or extraction filter. Once the TF domain polarization parameters are obtained by processing the RS-TFR of three-components through implementing the Eq. (19), a TF domain adaptive filter is designed based on the rectilinearity, directivity, and amplitude attributes to extract or remove different seismic wave phases.

2.3.1. Rectilinearity attribute

Rectilinearity is a critical parameter for discriminating between the elliptical and linear particle motion states. The purely rectilinear ground motion is modeled by one nonzero eigenvalue in the TF plane

$$\lambda_i(k,l) = 0, \;\; i > 1. \tag{24}$$

Nevertheless, due to the presence of contaminating noise, out-of-plane energy, and scattering distortions, it is seldom the case for the real data [30]. To circumvent it, a degree of rectilinearity

$$Re(k,l) = 1 - \frac{\lambda_2(k,l) + \lambda_3(k,l)}{\lambda_1(k,l)}, \tag{25}$$

is defined as a rectilinearity measure to discriminate between the rectilinear motion of Love and body waves and elliptical motion of Rayleigh waves [17], [31], [32]. Accordingly, a rectilinearity filter is designed in the TF domain as

$$\Psi_{Re}(k,l) = \begin{cases} 1 & -1 < Re(k,l) < \alpha \\ cos(\frac{\pi}{2(\beta-\alpha)}(Re(k,l) - \alpha)) & \alpha < Re(k,l) < \beta \\ 0 & \beta < Re(k,l) < 1, \end{cases} \tag{26}$$

while to avoid Aliasing phenomena caused by abrupt frequency cut-off, the accept or reject regions are cosine tapered in Eq. (24) by incorporating suitably defined adjusting parameters α and β. The proposed filter is similar to the TF filter introduced by [24], whereas it can be designed to filter the linear polarization particle motion.

2.3.2. Directivity and amplitude attributes

Directivity is another crucial parameters to discriminate between different seismic phases based on the direction of particle motion. Along with, the amplitude attribute can be combined to discriminate between the Love and body waves, specially SH waves, by cosidering a higher amplitude of Love waves in comparison to the body and coda waves [6]. More precisely, a directivity-amplitude (DA) measure is defined as dot product of the Semi-major (SM) axis by the base vectors

$$DA_i(k,l) = |\langle \frac{\sqrt{2}\lambda_1}{L} \boldsymbol{u}_1(k,l).\boldsymbol{e}_i\rangle|, \; i \in \{T, R, Z\}, \tag{27}$$

then normalizing the measure in the TF plane. The DA attribute is utilized to discriminate between the Love, Rayleigh, and also body and coda waves by considering both the direction of particle motion and a higher amplitude of the surface waves comparing the body waves. Correspondingly, a DA filter is designed in the TF domain as

$$\Psi_{DA}(DA_T(k,l)) = \begin{cases} 1 & 0 < DA_T(k,l) < \gamma \\ cos(\frac{\pi}{2(\lambda-\gamma)}(DA_T(k,l) - \gamma)) & \gamma < DA_T(k,l) < \lambda \\ 0 & \lambda < DA_T(k,l) < 1, \end{cases}$$

The adjusting parameters γ and λ have the role of both cosine tapering to avoid Aliasing and threshholding as a percentage of the maximum measure. In the next section we present the combination of these attribute to filter seismic data.

Table 1: $M_w = 6.7$ Prince Edward Islands region.

Date	Time	Latitude	Longitude	Depth
2019-01-22	19:01:43 (UTC)	-43.122°	42.357°	13.0 km

Table 2: Specifications of the seismic station in the synthetic simulation.

Net	Station	Lat	Lon	Dis	Azimuth	Elevation	Station name
GE	ACRG	5.64°	-0.21°	62.11°	-49.61°	75m	GEOFON/GGSA

2.3.3. Regularized Sparsity-promoting Time Frequency Filtering

To combine the properties of different attributes, a similar methodology to [24] can be followed. More precisely, the total time–frequency filter is obtained by combining the rectilinearity, Directivity-Amplitude filters, $\mathbf{\Psi}_{Re}$ and $\mathbf{\Psi}_{DA}$ in 24 and 2.3.2 as

$$\mathbf{\Psi} = 1 - \{1 - \mathbf{\Psi}_{Re}\} \circ \{1 - \mathbf{\Psi}_{DA}\}, \tag{28}$$

which $\circ$ operator in 28 denotes the Hadamard or element-wise product of matrices. The filtering process is applied by element-wise multiplication of $\mathbf{\Psi}$ with the RS-TFR of the three components; then, the filtered signal is reconstructed in the time domain by applying Eq. (20) giving the RS-TFF.

In the next section, we examine the application of the proposed filtering method to filter different seismic wave phases.

3. Numerical examples

To evaluate the RS-TFF method, we implement it on synthetic and real data examples to extract and filter the Love and Rayleigh waves. The implementation results are compared with those of the method introduced in Pinnegar [24].

3.1. Synthetic examples

The synthetic data corresponds to the source mechanism of the $M_w = 6.7$ Prince Edward Islands region earthquake occurred in the southeast of Africa continent, on January 22th, 2019, 19:01 UTC, as a result of normal faulting at the depth of 13.0 km [See Table. (1)]. This source mechanism corresponding to this event and the source-receiver geometry is chosen such that the amplitude of body and coda waves is almost comparable to the surface waves making separation more challenging. More precisely, due to the normal faulting mechanism, a low amplitude Love wave is generated. The station is chosen in a way to revive low amplitude Rayleigh waves according to the surface-wave distribution pattern [See Fig. 1].

A three-dimensional synthetic seismic data was generated through the 1D ak135f earth model [10] with spectral-element method assuming 3D (an-)elastic, anisotropic and acoustic wave propagation in spherical domains. The simulation was run by using the AxiSEM library through the IRIS Synthetics Engine (Syngine) client of ObsPy software [5, 10].

In the simulation, the seismic wavefield is recorded in the ACRG station in Accra, Ghana of GEOFON/GGSA seismic network [13] [See Table. (2) for more details], at the azimuth of $-49.61°$ to the epicenter.

The generated data was preprocessed; detrending and decimation by a factor of 8 were applied to attain a data set with a sampling rate of 0.5 sec. (A Butterworth anti-aliasing filter was applied prior to the decimation); then the traces were mapped to the transverse-radial-vertical coordinate system. To make the simulation more realistic, the data was contaminated by a Gaussian noise vector, $\boldsymbol{n} \in \mathbb{R}^{L \times 1}$, bandpass-filtered in the range $[0.02, 0.5]Hz$ to give a signal to noise ratio (SNR) of 10 according to

$$SNR = \frac{\sum_{l=0}^{L} x(l)^2}{\sum_{l=0}^{L} n(l)^2}. \tag{29}$$
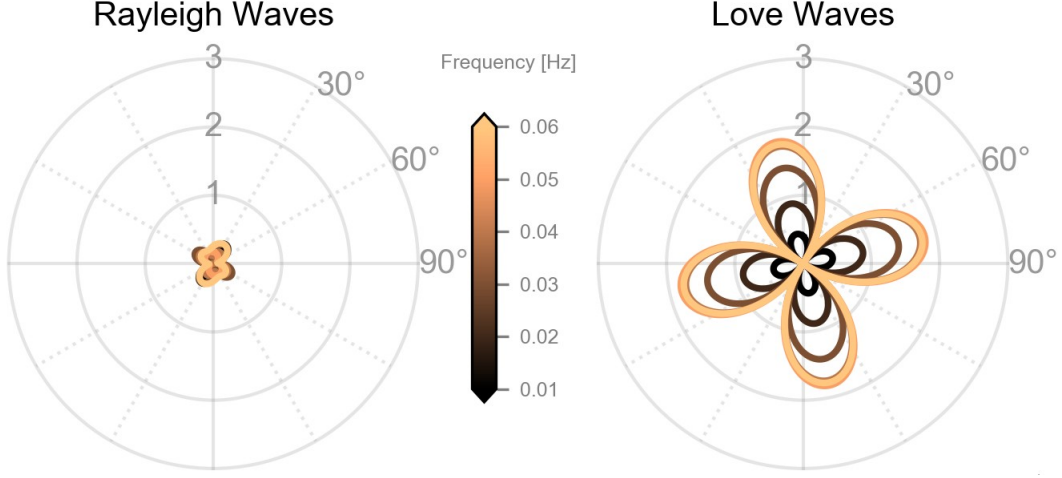
Figure 1: Surface-Wave Radiation Patterns $Mw = 6.7$ earthquake in Prince Edward Islands.

The Transverse, Radial, and Vertical components of the total motion are shown in Fig. (2).

To evaluate the efficiency of RS-TFF, the results are compared with the ones obtained by Pinnegar [24]. In this method, the ordinary ST is used as the TFR, and the TF-domain polarization parameters are obtained by fitting the particle motion to a parametric ellipse by incorporating the TFR of 3-components. More precisely, a set of the polarization parameters including $a(k, l)$ (the length of SM axis of the parametric ellipse), $b(k, l)$ (the length of Semi-minor (Sm) axis of the parametric ellipse), $I(k, l)$ (the inclination of the ellipse to the horizontal), $\Omega(k, l)$ (the azimuth of the ascending node, $\omega(k, l)$ (the angle between the ascending node and the position of maximum displacement) and $\phi(k, l)$ (the phase, measured with respect to the time of maximum displacement) are obtained, with $k = 0, ..., 2n + 1$ being the time and $l = 0, ..., n$ being the zero and positive frequency indices.

The TFR of the 3-components of the data obtained by the ordinary ST (applied by [24]) and the proposed RS-TFR are shown in the left and right panels of Fig. (3); the RS-TFR attains a highly compact TFR with a maximum amplitude higher than the ST, while ST distributed the energy in the TF plane in a wider area. The up-chirp characteristics of surface waves are obvious in both TFRs.

Fig. 4 depicts the TF domain SM and Sm axes of the particle motion obtained by [24] method (Left panel) and EDPA using RS-TFR (Right panels). The SM and Sm axes for EDPA is obtained as

$$
\begin{aligned}
SM(k, l) &= ||\boldsymbol{SM}(k, l)||_2 = \frac{\sqrt{2}\lambda_1}{L} ||\boldsymbol{u}_1(k, l)||_2, \\
Sm(k, l) &= ||\boldsymbol{Sm}(k, l)||_2 = \frac{\sqrt{2}\lambda_2}{L} ||\boldsymbol{u}_2(k, l)||_2,
\end{aligned}
\tag{30}
$$

with k and l are defined similar to Eq. (16). The left panels of Figs. (3) and (4) indicate that using the ordinary ST, the Rayleigh and Love waves are inseparably overlapping both in time and frequency. In contrast, for the RS-TFR (Right panels), the high-resolution TFR highly separated the wavefields, giving the possibility to discriminate between different seismic wave phases. By incorporating the obtained TF domain polarization parameters, we process the data to filter different phases of seismsic phases.

3.1.1. Love and Rayleigh wave elimination using RS-TFF

In a laterally homogeneous structure, the Love wave appears mostly on the transverse component and the Rayleigh waves mostly appears on the vertical and radial components [42]. However, in the real data due to the laterally heterogeneous and anisotropic propagation environment and contaminating noise, it is seldom the case. Furthermore, it is always a challenge to discriminate between the body and Rayleigh waves on the vertical and radial components and SH and Love waves on the transverse component. The TF
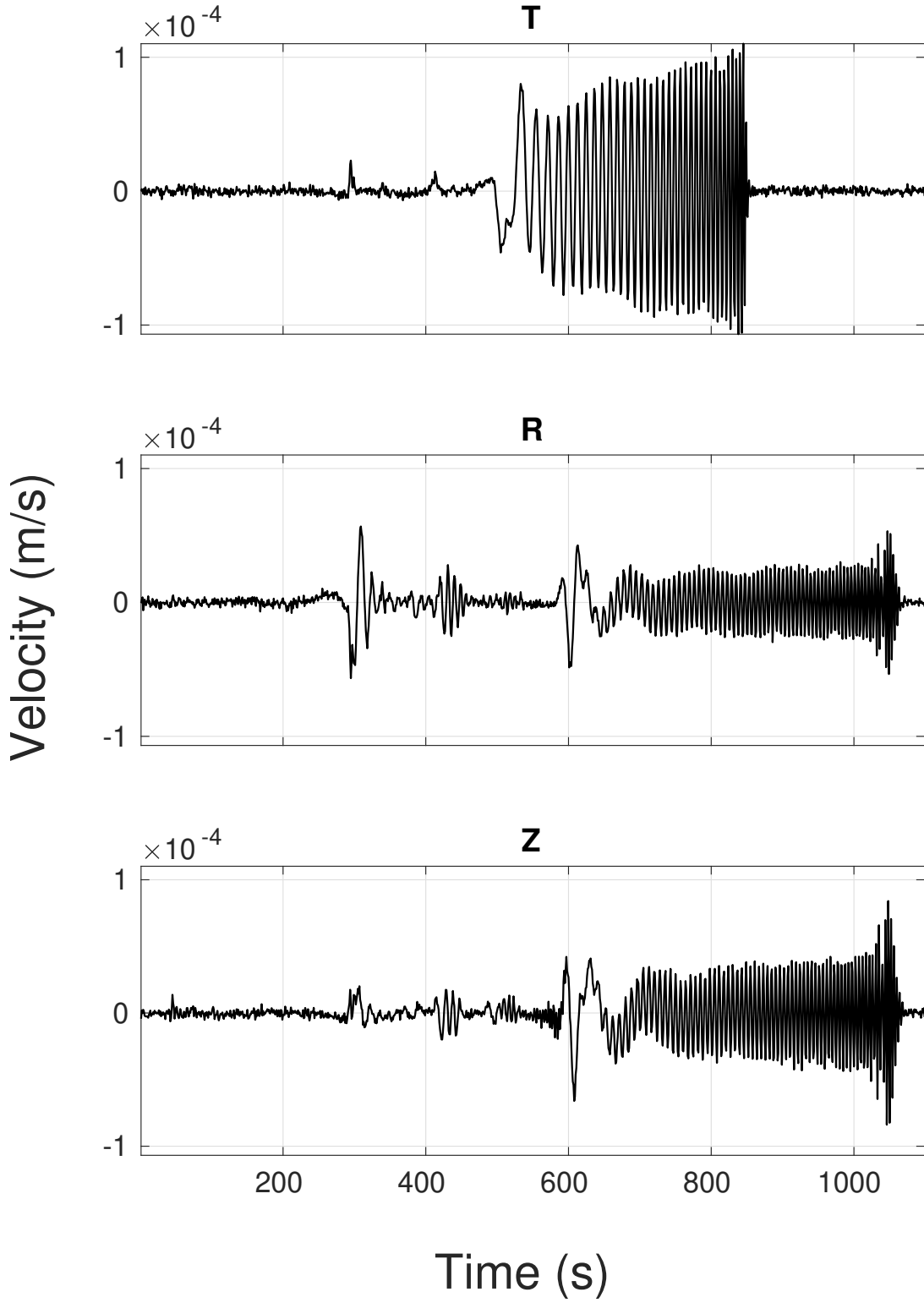
9

Figure 2: A 3D synthetic seismogram genterated for the source mechanism of $M_w = 6.7$ Prince Edward Islands region earthquake, by using the IRIS Syngine client of ObsPy through the 1D ak135f earth model [See text and Table. 1], recorded in ACRG station GEOFON seismic network.
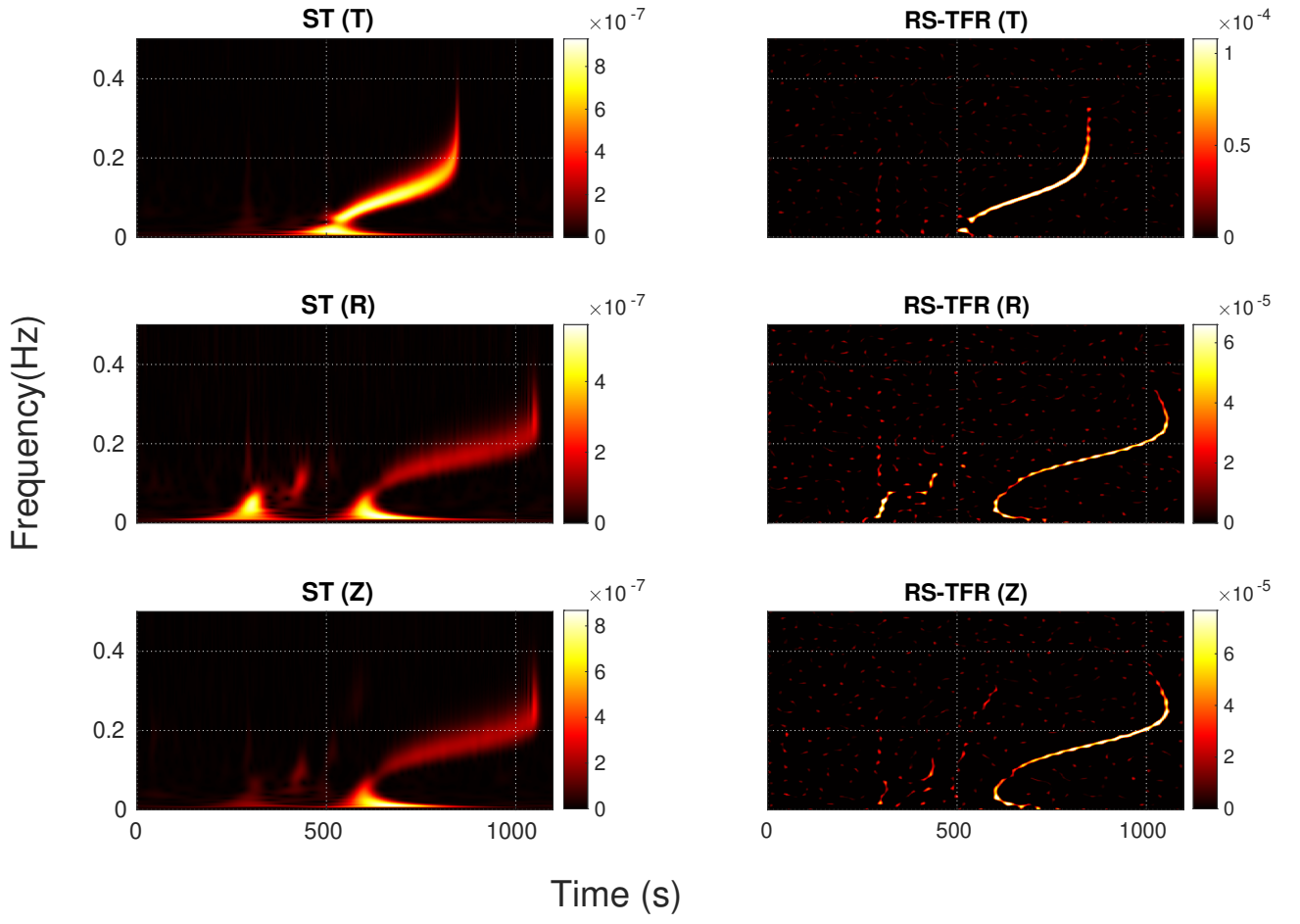
Figure 3: Left panel: The TFR of the transverse, radial, and vertical compenents of the ACRG synthetic seismogram obtained by applying conventional ST. Right panel: The RS-TFR of the components.
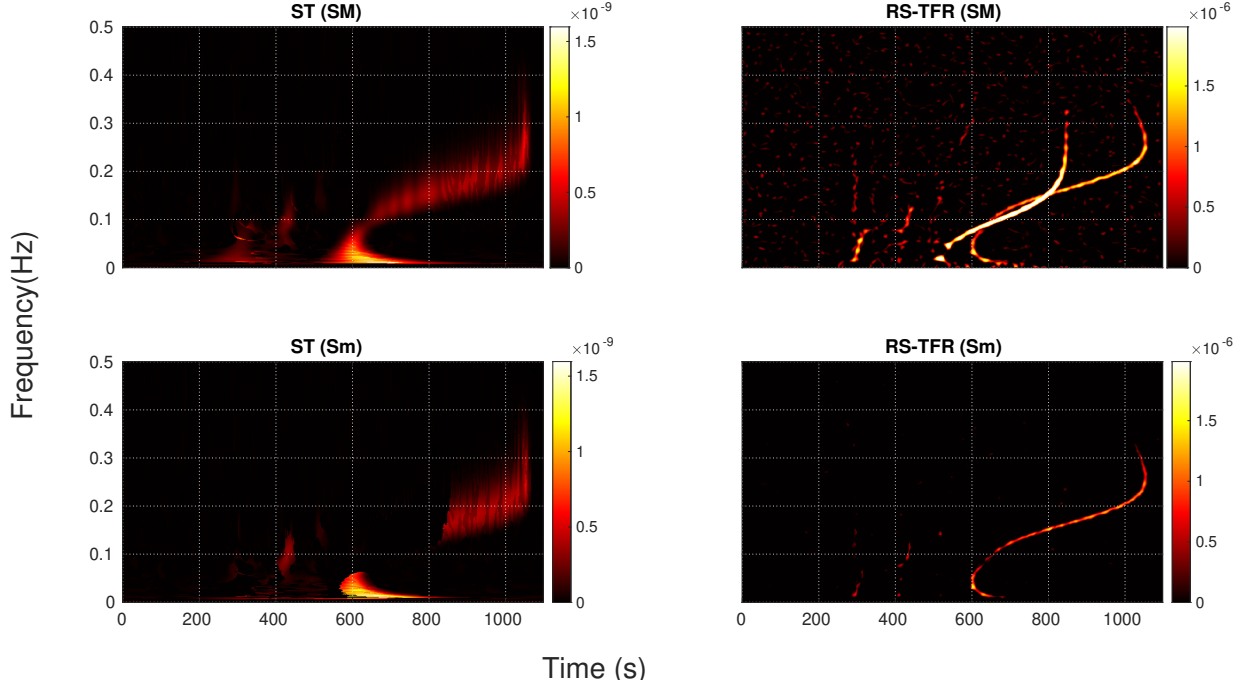
Figure 4: Left panel: The TFR of the length of the SM and Sm axis of particle motion obtained by using the [24] method. Right: SM and Sm axes by implementing EDPA on the RS-TFR.

domain polarization parameters obtained form RS-TFR, are used to define and adaptive filter according to section (2.3) to filter Love and Rayleigh waves.

To extract and filter the Love waves, we define a DA filter by computing the directivity measure with respect to the transverse axis $\boldsymbol{e}_T$ in Eq. (27), and a set of adjusting parameters $\gamma = 0.13$ and $\lambda = 0.22$ for amplitude threshholding and cosine tapering the DA measure; the results of applying the filter on the RS-TFRs of o 3-components are shown in left panel of Fig. (5). As it is shown, the energy corresponds to the Love wave in the TF plane has been significantly removed, and only scattered energy remains, which corresponds to the body and coda waves, and noise (top panel). The RS-TFRs of the radial (middle panel) and vertical (bottom panel) components have not gotten affected by filtering. The left panels of Fig. (6) depict reconstructed components of filtered signal in the time domain; the Love wave is almost entirely removed in the time domain, while the other phases, including the body and coda wave, and also the noise has remained in the seismogram. It is a promising feature of the RS-TFF algorithm compared to the Pinnegar [24] method, which attains a null value for the inclination and azimuth parameters corresponding to a linear particle motion. The filtering process has not affected other phases in the radial and vertical components, except a minor effect on the Rayleigh phase around the time 800s, in which the RS-TFR of the Rayleigh and Love phases fully overlaps.

To filter the Rayleigh phase, the directivity measure is computed with respect to the radial-vertical plane computed as

$$DA(k,l) = \sqrt{DA_R(k,l)^2 + DA_Z(k,l)^2}. \tag{31}$$

The adjusting parameters are set to $\gamma = 0.25$ and $\lambda = 0.3$. Furthermore, a rectilinearity filter is defined by setting the parameters $\alpha = 0.2$ and $\beta = 0.4$; the results of applying the filter on the RS-TFRs of o 3-components are shown in the right panels of Fig. (6). Similar to the Love wave filtering, the filtered RS-TFR only contains scattered energy of the noise, body and coda waves in the radial and vertical components. The reconstructed filtered components are shown in the right panels of shown in the right panel of Fig. (6).
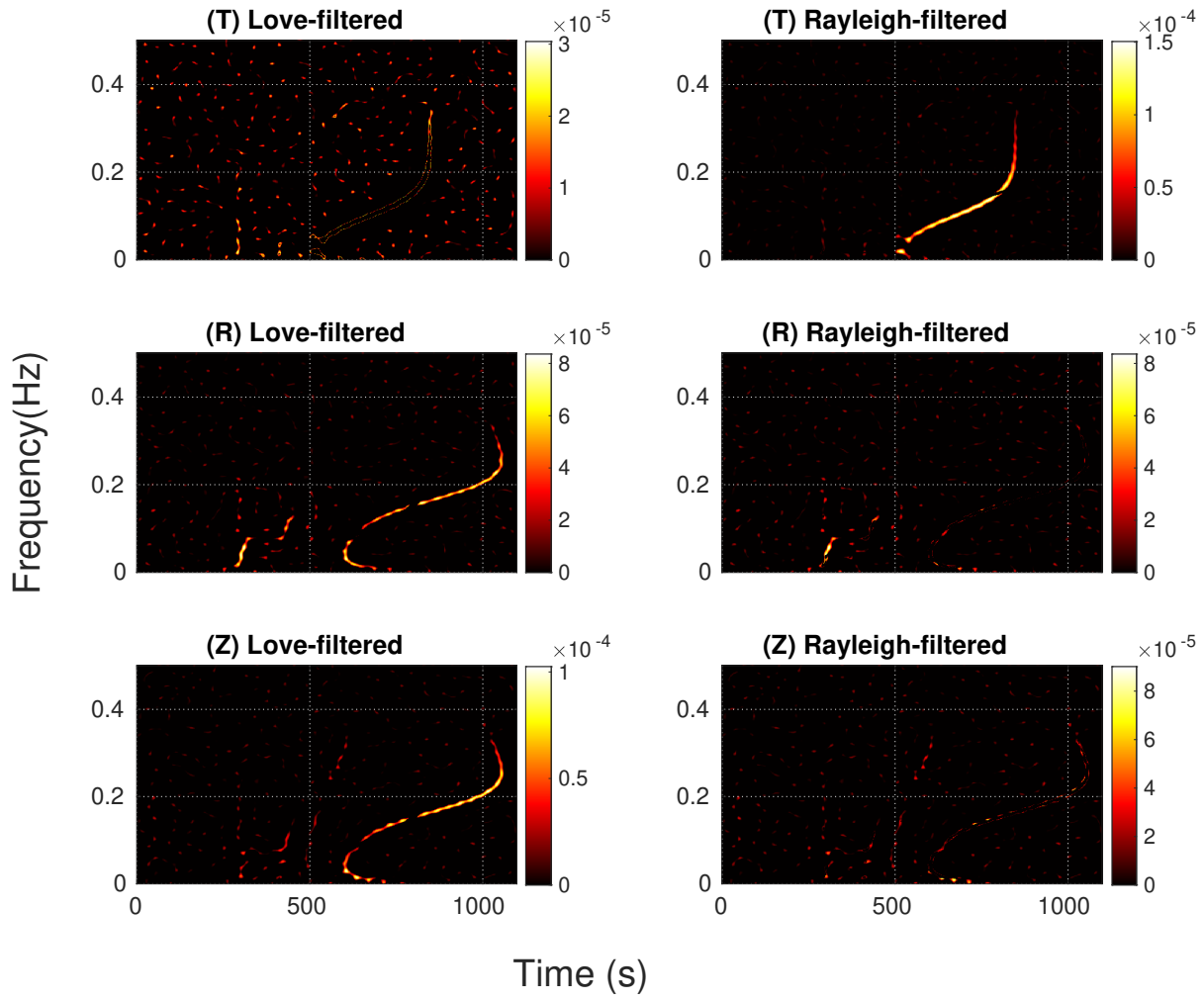
12

Figure 5: Left panel: Adaptively Filtered RS-TFRs of the transverse, radial, and vertical components of synthetic data to eliminate the Love wave. Right panel: Adaptively Filtered RS-TFRs of components to eliminate the Rayleigh wave. (5).
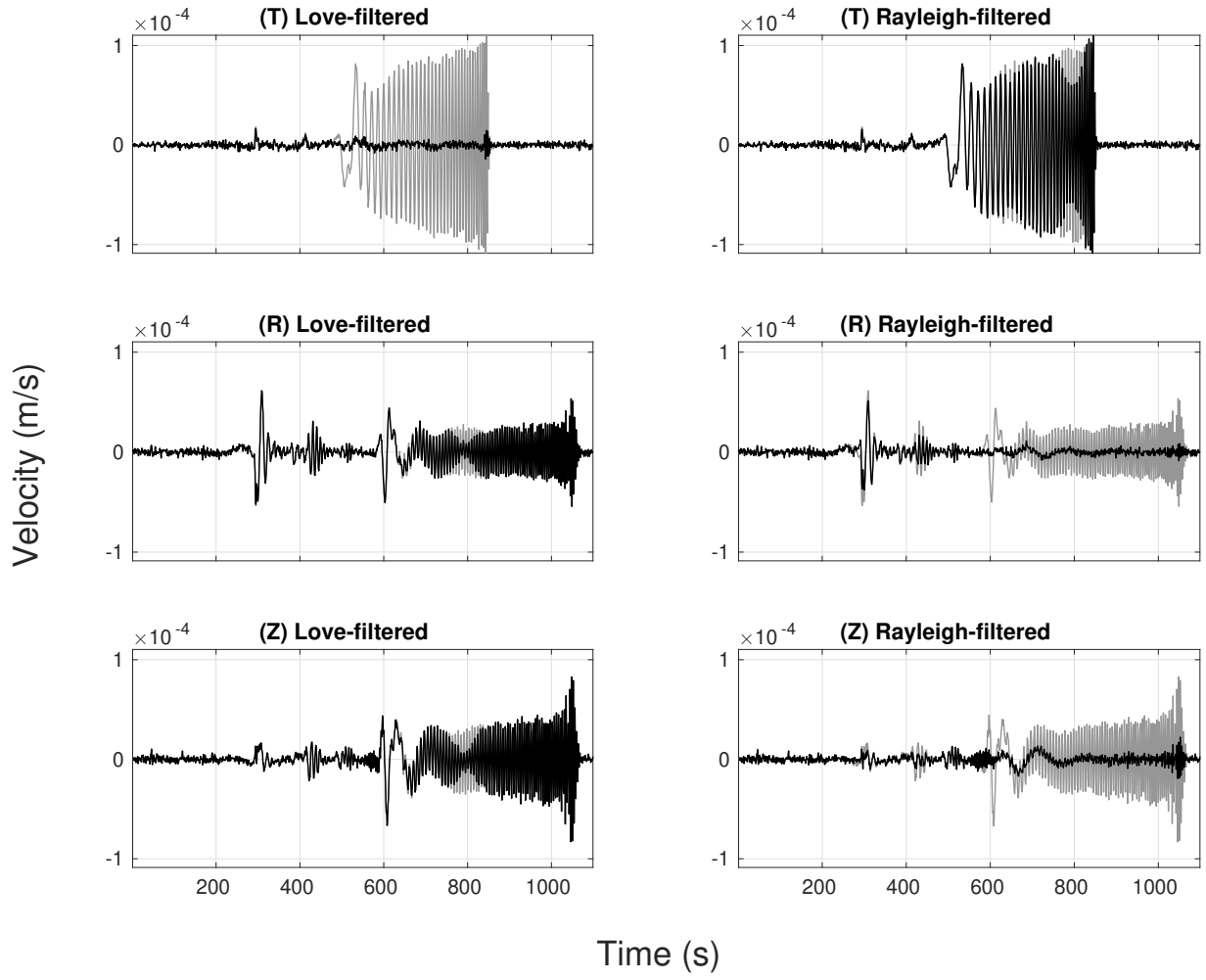
Figure 6:   Left panel: The filtered transverse, radial, and vertical components by using the RS-TFF to eliminate the Love wave. Right panel: The filtered transverse, radial, and vertical components by using the RS-TFF to eliminate the Rayleigh wave.

Table 3: $M_w = 8.2$ near Coast Of Chiapas, Mexico

Date	Time	Latitude	Longitude	Depth
2017-09-08	04:49:20 UTC	15.022	-93.899	47.4km

Table 4: Specifications of the seismic station recorded the $M_w = 8.2$ earthquake near Coast Of Chiapas, Mexico simulation.

Net	Station	Lat	Lon	Dis	Azimuth	Elevation	Station name
IU	COLA	64.87°	-147.86°	61.56°	-22.98°	200m	COLA: College Outpost, Alaska, USA

As shown, RS-TFF successfully filtered the Rayleigh wave without affecting the body and coda waves in the radial and vertical components and having a substantial effect on the other phases in the transverse components. The same as for the Love wave filtering, around 800s, the Love wave has slightly been filtered. The obtained results of RS-TFF is superior to the Pinnegar [24] by having a very high-resolution TFR to separate the Rayleigh and Love waves, as in the ordinary ST the TF resolution is limited.

3.2. Real data example

The real seismogram corresponds to the $M_w = 8.2$ earthquake that occurred near the coast of Chiapas, Mexico, on September 8th, 2017, 04:49:19 (UTC), as a result of normal faulting at the depth 47.0 km [See Table. (3)]. The waveform has been recorded with the COLA seismic station of the Global Seismograph Network seismic network [2] at College Outpost, Alaska, USA. The station is in 61.56° distance of the epicenter [See Table. (4) for more details]. The waveform was pre-processed; detrending and decimation were applied, the instrument response was deconvolved, and the data was converted to velocity with a sampling rate of 2 sec. The traces were mapped to the transverse-radial-vertical coordinate system. The pre-processed 3-component seismogram is shown in Fig. (7).

The obtained TFR by applying [24]) and RS-TFR methods are shown in the left and right panels of Fig. (8); the same as for the synthetic data, the RS-TFR presents a highly compact TFR comparing to the ordinary ST implemented by [24]. Although there is no sharp up-chirp pattern for the surface waves like in the synthetic data, there are still two separate energy panels in the RS-TFR of different components showing an increasing value of frequency by time. These two panels marked by green and blue ovals correspond to Love and Rayleigh waves, respectively. Two other panels shown by white ovals contain mostly body and coda waves. On the other hand, the TFR obtained by ST and shown in the left panel of Fig. (8) depicts a mixed and inseparable pattern of Love and Rayleigh waves. The distinct polarization pattern between the Love and Rayleigh waves is better visible in the TF domain SM and Sm axes of particle motion as shown in the right panel of Fig. (9). The elliptical particle motion of Rayleigh waves is separable from the Linear particle motion of Love, body, and coda waves in the SM and Sm axes figures. Contrarily, they have been mixed in time and frequency in the results obtained by Pinnegar [24] method, as can be seen in the left panel of Fig. (9). In the next subsection, we present the adaptive filtering method results to filter the Love and Rayleigh waves.

3.2.1. Love and Rayleigh wave elimination using RS-TFF

The TF domain polarization parameters obtained from RS-TFR are used to design an adaptive filter to filter Love and Rayleigh waves. For the real data, the DA filter is defined by setting adjusting parameters $\gamma = 0.27$ and $\lambda = 0.29$ for amplitude threshholding and cosine tapering the DA measure; The left panel of Fig. (10) shows the filtered RS-TFRs of o 3-components. As it can be seen, the focused energy corresponding to the Love waves (shown by blue oval in Figs. (9)and (8)) are highly damped due to DA filtering, and only a scattered signal corresponding to body and coda waves remained in the transverse component. The RS-TFRs of the radial (middle panel) and vertical (bottom panel) components have not gotten affected by filtering. The left panels of Fig. (11) depict reconstructed components of filtered signal in the time domain; the results shows that the DA amplitude highly removed the Love wave time domain without affecting the othre phases including the body and coda waves.
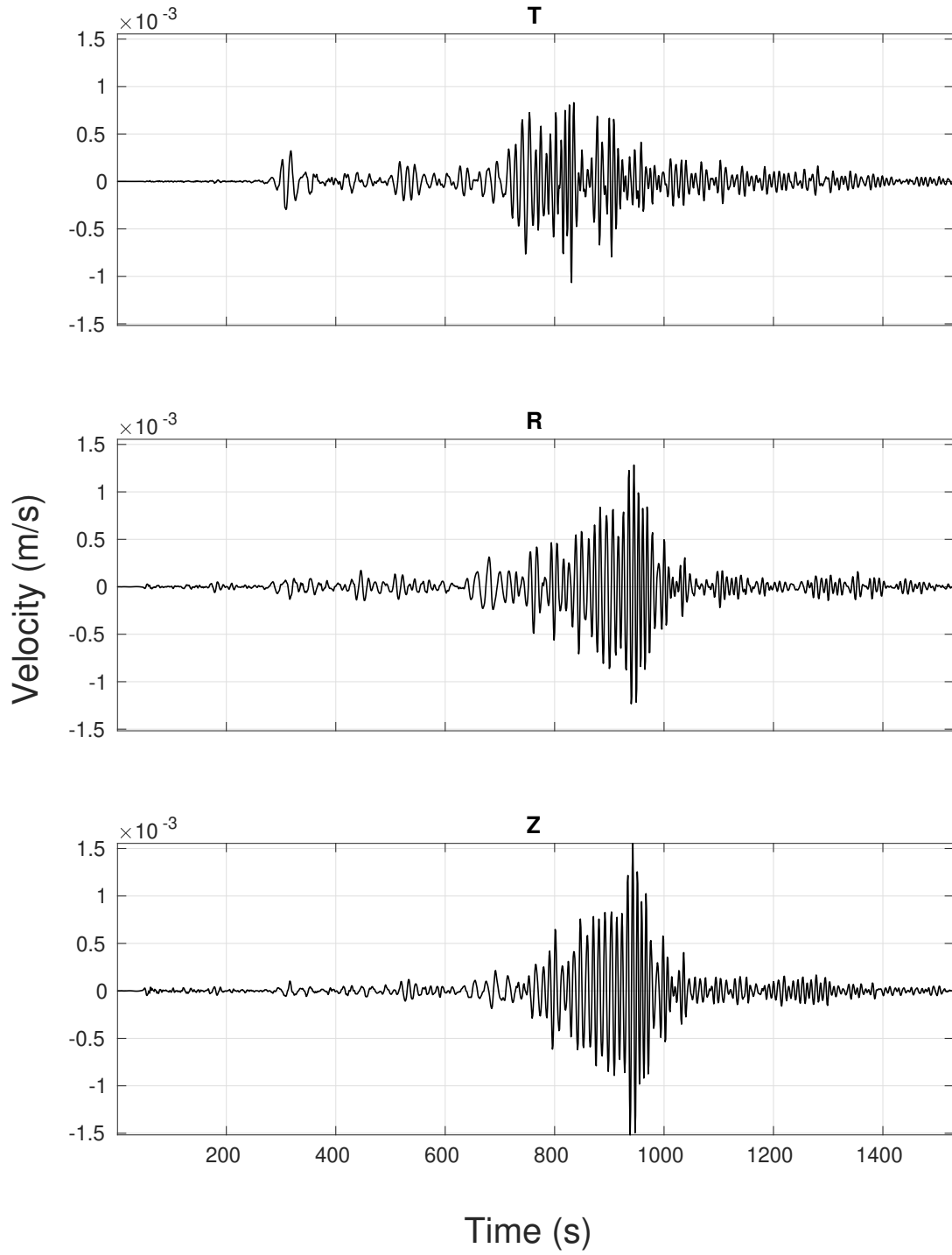
Figure 7: A real seismogram corresponds to the $M_w = 8.2$ earthquake occurred near the coast of Chiapas, Mexico, on September 8th, 2017. The waveform has been recorded with the COLA station of the IU seismic network at College Outpost, Alaska, USA.
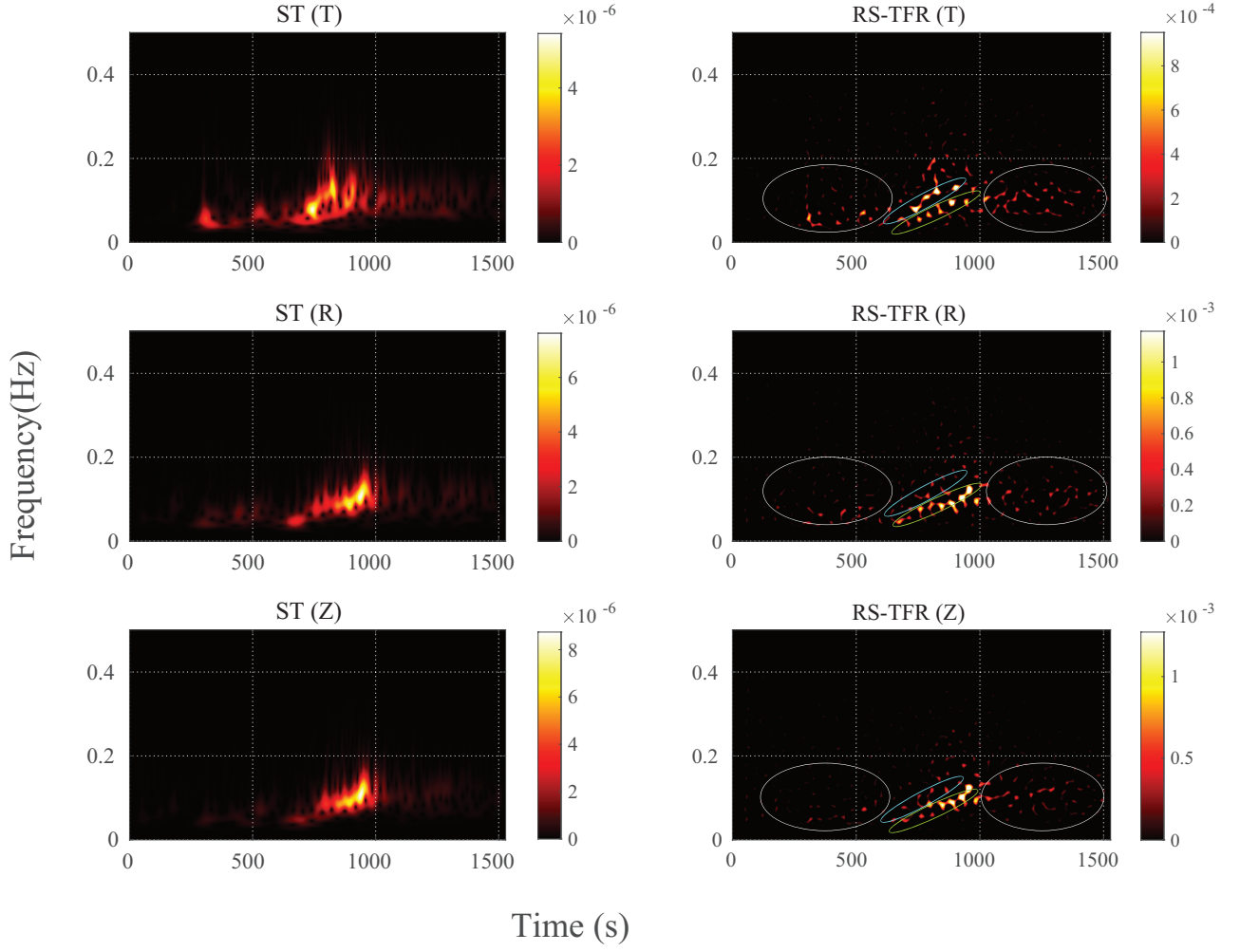
Figure 8: Left panel: The TFR of the transverse, radial, and vertical compenents of $M_w = 8.2$ earthquake obtained by applying conventional ST. Right panel: The RS-TFR of the components.
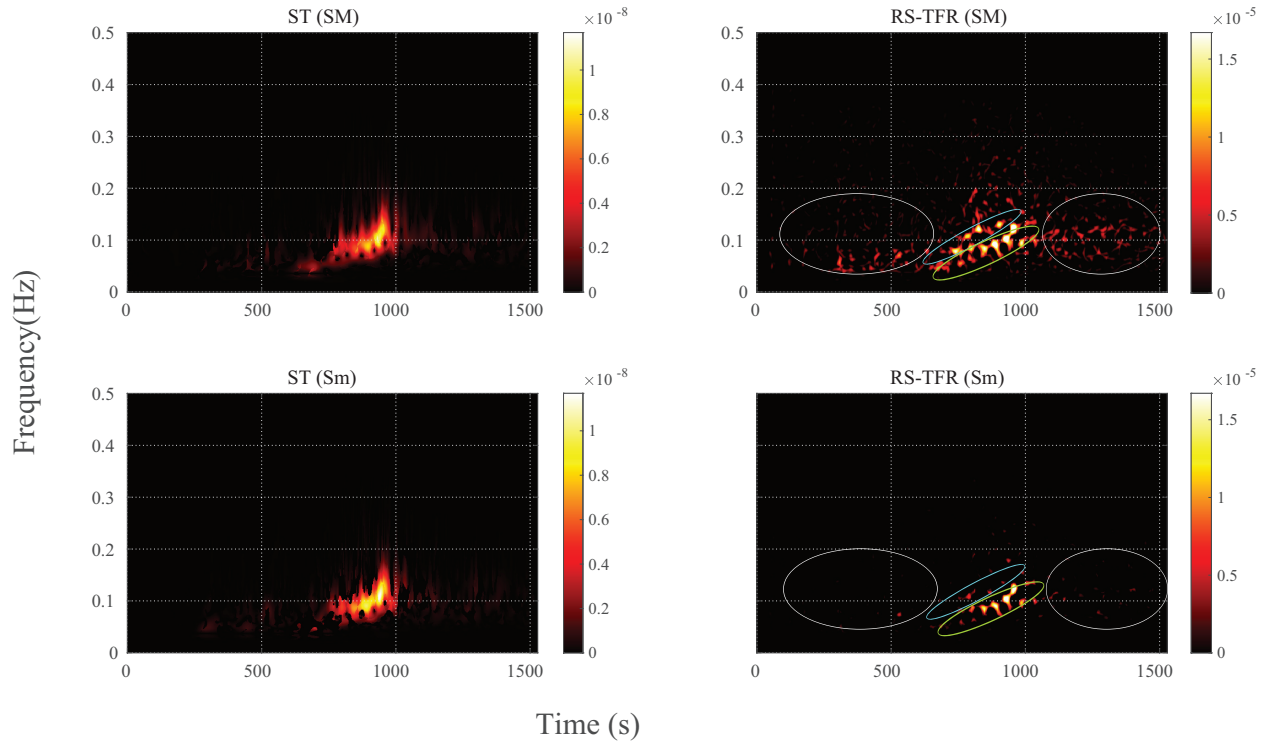
Figure 9: Left panel: The TFR of the length of the SM and Sm axis of particle motion of the transverse, radial, and vertical components of $M_w = 8.2$ earthquake obtained by using the [24] method. Right: SM and Sm axes by implementing EDPA on the RS-TFR.

To filter the Rayleigh phase, the adjusting parameters of the directivity measure are set to $\gamma = 0.1$ and $\lambda = 0.13$, and the rectilinearity filter is set to have $\alpha = 0.02$ and $\beta = 0.04$ adjusting parameters. The results of applying the filter on the RS-TFRs of o 3-components are shown in the right panels of Fig. (10). Similar to the Love wave filtering, the filtered RS-TFR only contains scattered energy of the noise, body and coda waves in the radial and vertical components. The reconstructed filtered components are shown in the right panels of shown in the right panel of Fig. (11). As shown, RS-TFF successfully filtered the Rayleigh wave without affecting the body and coda waves in the radial and vertical components and having a substantial effect on the other phases in the transverse components.

4. Discussion

In numerical examples including synthetic and real data we showed that the RS-TFR can be used as a sophisticated tool to separate different phases of seismic waves according to their state of polarization. Taking advantageous of sparsity-promoting regularized time-frequency estimation, the method attains a high resolution for resolving closely spaces seismic events in time and frequency. Combining RS-TFR and EDPA, the method is able to filter eliptical and linear particle motion by designing suitably defined directivity, rectilinearity, and amplitude attributes. The research work can advance by applying the RS-TFF to seismic data made by more realistic numerical simulations, including 3D non-homogeneous and anisotropic earth models. RS-TFF can find applications in more accurately estimating the seismic anisotropy parameters obtained from the the Shear Wave Splitting method. It can also be used to extract surface waves as an input to surface wave dispersion curve inversion methods. Furthermore, it can act as a promising tool to eliminate the surface waves to prepare the earthquake data for coda waves studies [44]. A high computation part of the algorithm includes solving the regularized inverse problems. (22) and (23). For a large data set, it need a high computation time and memory space. Notwithstanding, it can be accounted as a drawback for the RS-TFF method comparing to the other conventional polarization filtering methods.

5. Conclusions

We presented a RS-TFF approach for the EDPA of three-component seismic signals: The method computes a high-resolution TF domain information of polarization state of the signal in terms of eigenvalues and eigenvectors. The extracted information combined by rectilineary, directivity, and amplitude filtering is utilized to extract and filter different phases of seismic waves, including Rayleigh and Love waves. The proposed procedure is a clear improvement over similar polarization analysis and filtering methods like Pinnegar [24] in recognizing and filtering the linear polarization motions and discriminating between closely spaced seismic phases in time and frequency.

6. Code and data availability

The numerical synthetic and real data examples presented in this paper is reproducible by running a set of Python codes available at the Github account ("Will be inserted when the manuscript is accepted").

7. Acknowledgments

Appendix A. acronyms

TF time-frequency

TFR time-frequency representation

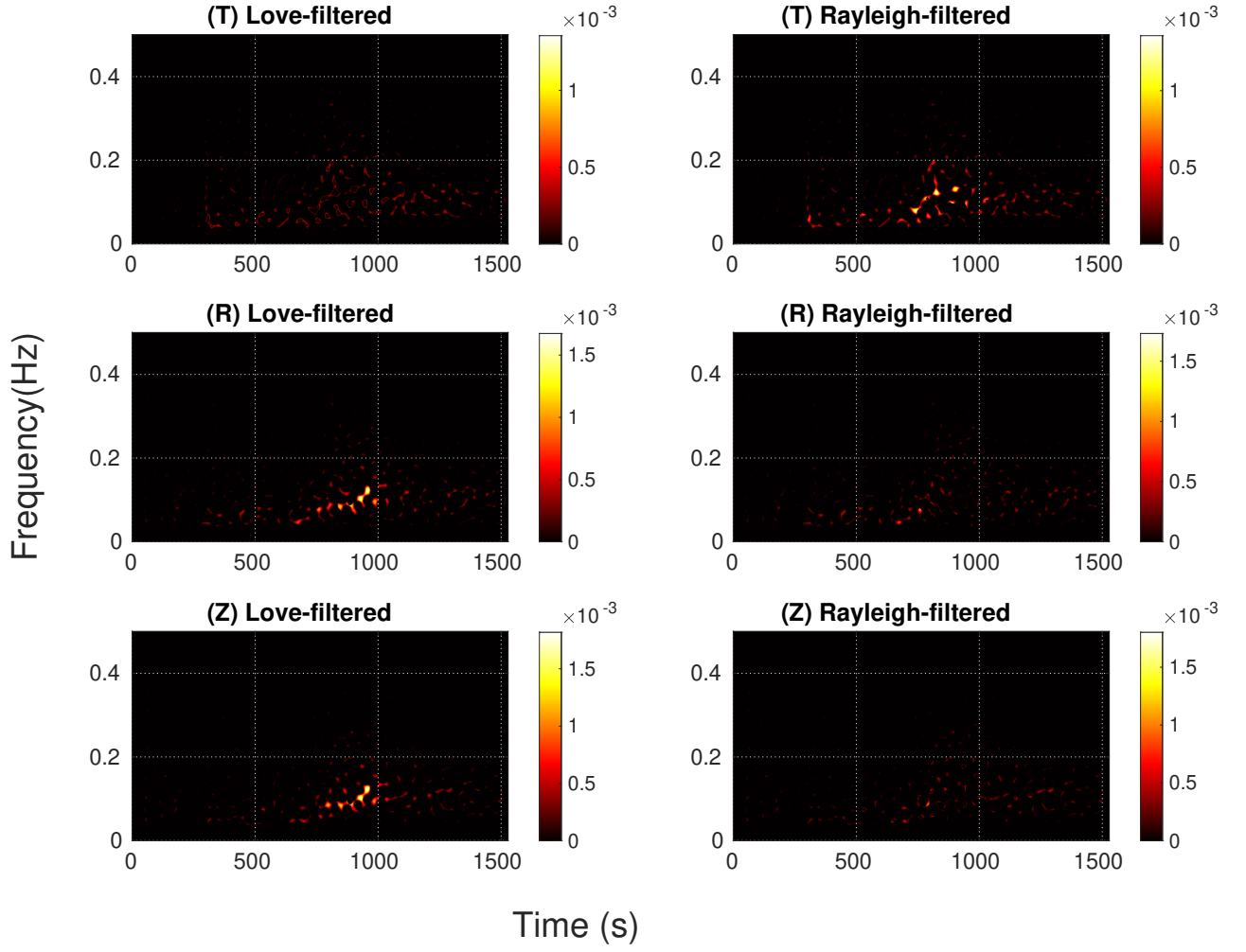**RS-TFR** regularized sparsity-promoting time-frequency representation

Figure 10: Left panel: Adaptive Filtered RS-TFRs of the transverse, radial, and vertical components of the $M_w = 8.2$ earthquake to eliminate the Love wave. Right panel: Adaptive Filtered RS-TFRs of components to eliminate the Rayleigh wave.
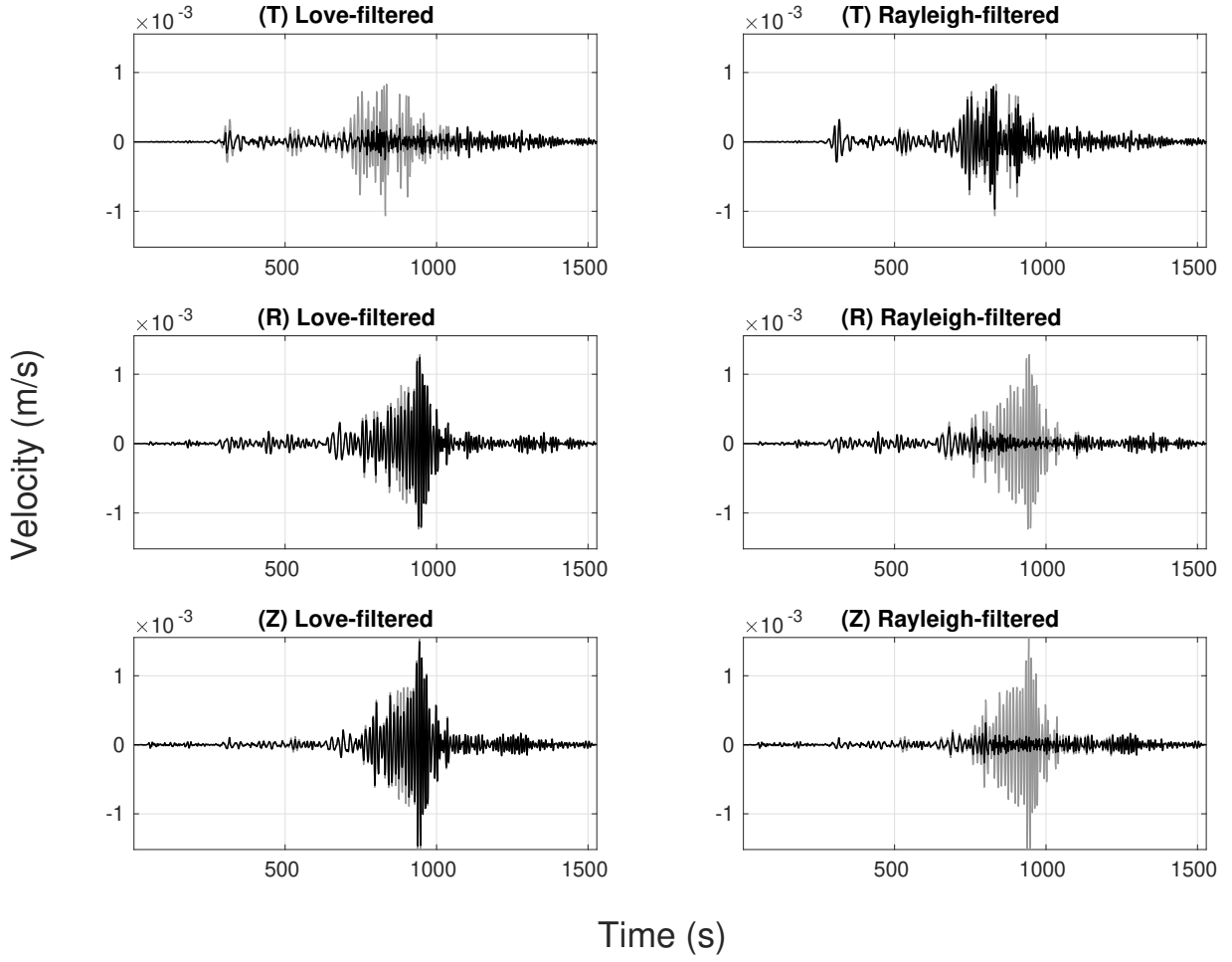
Figure 11: Left panel: The filtered transverse, radial, and vertical components of the $M_w = 8.2$ earthquake to eliminate the Love wave. Right panel: The filtered transverse, radial, and vertical components by using the RS-TFF to eliminate the Rayleigh wave.

RS-TFF regularized sparsity-promoting time-frequency filtering

DOP degree of polarization

FISTA fast iterative soft thresholding algorithm

KKT Karush–Kuhn–Tucker

IRLS iteratively reweighted least squares

STFT short time fourier transform

ST Stockwell transform

WT Wavelet transform

TSR time-scale representation

SST synchrosqueezing transform

SM Semi-major

Sm Semi-minor

EDPA eigenvalue decomposition polarization analysis

DA directivity-amplitude

SNR signal to noise ratio

References

[1] Aki, K., Richards, P.G., 2002. Quantitative seismology.

[2] Albuquerque Seismological Laboratory (ASL)/USGS, 1988. Global seismograph network (gsn - iris/usgs). URL: `http://www.fdsn.org/doi/10.7914/SN/IU`, doi:`10.7914/SN/IU`.

[3] Allen, J., 1977. Short term spectral analysis, synthesis, and modification by discrete fourier transform. IEEE Transactions on Acoustics, Speech, and Signal Processing 25, 235–238. doi:`10.1109/TASSP.1977.1162950`.

[4] Beck, A., Teboulle, M., 2009. A fast iterative shrinkage-thresholding algorithm for linear inverse problems. SIAM journal on imaging sciences 2, 183–202.

[5] Beyreuther, M., Barsch, R., Krischer, L., Megies, T., Behr, Y., Wassermann, J., 2010. Obspy: A python toolbox for seismology. Seismological Research Letters 81, 530–533.

[6] Bolt, B.A., Bolt, B.A., 1982. Inside the Earth: Evidence from earthquakes. WH Freeman San Francisco.

[7] Chen, S.S., Donoho, D.L., Saunders, M.A., 2001. Atomic decomposition by basis pursuit. SIAM review 43, 129–159.

[8] Daubechies, I., Lu, J., Wu, H.T., 2011. Synchrosqueezed wavelet transforms: An empirical mode decomposition-like tool. Applied and computational harmonic analysis 30, 243–261.

[9] Diallo, M.S., Kulesh, M., Holschneider, M., Scherbaum, F., Adler, F., 2006. Characterization of polarization attributes of seismic waves using continuous wavelet transforms. Geophysics 71, V67–V77.

[10] van Driel, M., Hutko, A., Krischer, L., Trabant, C., Stähler, S., Nissen-Meyer, T., 2016. Syngine: on-demand synthetic seismograms from the iris dmc based on axisem & instaseis, in: EGU General Assembly Conference Abstracts, pp. EPSC2016–8190.

[11] Flandrin, P., 1998. Time-frequency/time-scale analysis. Academic press.

[12] Flinn, E., 1965. Signal analysis using rectilinearity and direction of particle motion. Proceedings of the IEEE 53, 1874–1876.

[13] GEOFON Data Centre, 1993. Geofon seismic network. URL: `http://geofon.gfz-potsdam.de/doi/network/GE`, doi:`10.14470/TR560404`.

[14] Gholami, A., 2012. Sparse time–frequency decomposition and some applications. IEEE Transactions on Geoscience and Remote Sensing 51, 3598–3604.

[15] Gorodnitsky, I.F., Rao, B.D., 1997. Sparse signal reconstruction from limited data using focuss: A re-weighted minimum norm algorithm. IEEE Transactions on signal processing 45, 600–616.

[16] Jones, J.P., Eaton, D.W., Caffagni, E., 2016. Quantifying the similarity of seismic polarizations. Geophysical Journal International 204, 968–984.

[17] Jurkevics, A., 1988. Polarization analysis of three-component array data. Bulletin of the seismological society of America 78, 1725–1743.

[18] Kulesh, M., Diallo, M., Holschneider, M., Kurennaya, K., Krüger, F., Ohrnberger, M., Scherbaum, F., 2007. Polarization analysis in the wavelet domain based on the adaptive covariance method. Geophysical Journal International 170, 667–678.

[19] Kyparisis, J., 1985. On uniqueness of kuhn-tucker multipliers in nonlinear programming. Mathematical Programming 32, 242–246.

[20] Lay, T., Wallace, T.C., 1995. Modern global seismology. Elsevier.

[21] Lu, J., Wang, Y., Yang, C.Y., 2010. Instantaneous polarization filtering focused on suppression of surface waves. Applied Geophysics 7, 88–97.

[22] Mallat, S., 1999. A wavelet tour of signal processing. Elsevier.

[23] Montalbetti, J.F., Kanasewich, E.R., 1970. Enhancement of teleseismic body phases with a polarization filter. Geophysical Journal International 21, 119–129.

[24] Pinnegar, C., 2006. Polarization analysis and polarization filtering of three-component signals with the time—frequency s transform. Geophysical Journal International 165, 596–606.

[25] Pinnegar, C.R., Eaton, D.W., 2003. Application of the s transform to prestack noise attenuation filtering. Journal of Geophysical Research: Solid Earth 108.

[26] Plešinger, A., Hellweg, M., Seidl, D., et al., 1986. Interactive high-resolution polarization analysis of broad-band seismograms. Journal of Geophysics| IF 32.18 59, 129–139.

[27] Portniaguine, O., Castagna, J., 2004. Inverse spectral decomposition, in: SEG Technical Program Expanded Abstracts 2004. Society of Exploration Geophysicists, pp. 1786–1789.

[28] Samson, J., 1973. Descriptions of the polarization states of vector processes: applications to ulf magnetic fields. Geophysical Journal International 34, 403–419.

[29] Samson, J., Olson, J., 1980. Some comments on the descriptions of the polarization states of waves. Geophysical Journal International 61, 115–129.

[30] Sato, H., Fehler, M.C., Maeda, T., 2012. Seismic wave propagation and scattering in the heterogeneous earth. Springer Science & Business Media.

[31] Schimmel, M., Gallart, J., 2003. The use of instantaneous polarization attributes for seismic signal detection and image enhancement. Geophysical Journal International 155, 653–668.

[32] Schimmel, M., Gallart, J., 2004. Degree of polarization filter for frequency-dependent signal enhancement through noise suppression. Bulletin of the Seismological Society of America 94, 1016–1035.

[33] Schimmel, M., Stutzmann, E., Ardhuin, F., Gallart, J., 2011. Polarized earth's ambient microseismic noise. Geochemistry, Geophysics, Geosystems 12.

[34] Simons, R., 1968. A surface wave particle motion discrimination process. Bulletin of the Seismological Society of America 58, 629–637.

[35] Stephane, M., 1999. A wavelet tour of signal processing.

[36] Stockwell, R.G., 2007. A basis for efficient representation of the s-transform. Digital Signal Processing 17, 371–393.

[37] Tan, Y.Y., He, C., Wang, Y.D., Zhao, Z., 2013. Ground roll attenuation using a time-frequency dependent polarization filter based on the s transform. Applied Geophysics 10, 279–294.

[38] Tary, J., Herrera, R., Van der Baan, M., 2014. Time-varying autoregressive model for spectral analysis of microseismic experiments and long-period volcanic events. Geophysical Journal International 196, 600–611.

[39] Tikhonov, A.N., Goncharsky, A., Stepanov, V., Yagola, A.G., 2013. Numerical methods for the solution of ill-posed problems. volume 328. Springer Science & Business Media.

[40] Ventosa, S., Simon, C., Schimmel, M., Dañobeitia, J.J., Mànuel, A., 2008. The s-transform from a wavelet point of view. IEEE Transactions on Signal Processing 56, 2771–2780.

[41] Vera Rodriguez, I., Bonar, D., Sacchi, M., 2012. Microseismic data denoising using a 3c group sparsity constrained time-frequency transform. Geophysics 77, V21–V29.

[42] Vidale, J.E., 1986. Complex polarization analysis of particle motion. Bulletin of the Seismological society of America 76, 1393–1405.

[43] Wang, C., Wang, Y., Sun, P., Li, Y., 2019. Discussions on the processing of the multi-component seismic vector field. Applied Sciences 9, 1770.

[44] Wang, W., Shearer, P., 2017. Using direct and coda wave envelopes to resolve the scattering and intrinsic attenuation structure of southern california. Journal of Geophysical Research: Solid Earth 122, 7236–7251.